

## Solubilization of saikosaponin a by ginsenoside Ro biosurfactant in aqueous solution: Mesoscopic simulation

Xingxing Dai<sup>a,1</sup>, Xinyuan Shi<sup>b,c,d,\*</sup>, Yuguang Wang<sup>a</sup>, Yanjiang Qiao<sup>b,c,d,\*</sup>

<sup>a</sup> School of Traditional Chinese Medicine, Capital Medical University, Beijing 100069, China

<sup>b</sup> Beijing University of Chinese Medicine, Beijing 100102, China

<sup>c</sup> Key Laboratory of TCM-Information Engineer of State Administration of TCM, Beijing 100102, China

<sup>d</sup> Beijing Key Laboratory for Basic and Development Research on Chinese Medicine, Beijing 100102, China

### ARTICLE INFO

#### Article history:

Received 8 March 2012

Accepted 8 June 2012

Available online 18 June 2012

#### Keywords:

Biosurfactant

Ginsenoside Ro

Saikosaponin a

Solubilization

Mesoscopic simulation

Vesicle

### ABSTRACT

Ginsenoside Ro (Ro), a natural anionic biosurfactant derived from ginseng, has been found to markedly increase the solubility of saikosaponin a (SSa), which is the active ingredient of *Radix Bupleuri*. SSa is minimally soluble in water. To determine the mechanism by which Ro solubilizes SSa, the self-assembly behavior of Ro and the phase behavior of blended Ro and SSa systems were studied by mesoscopic dynamics (MesoDyn) and dissipative particle dynamics (DPD) simulations. The simulation results show that Ro can form vesicles via the closure of oblate membranes. At low concentrations, SSa molecules are solubilized in the palisade layer of the Ro vesicles. At high concentrations, they interact with Ro molecules to form mixed vesicles with Ro adsorbing on the surfaces of the vesicles. The evaluation of the SSa solubilization process reveals that, at low concentrations, Ro aggregates preferentially to form vesicles, which then absorb SSa into themselves. However, at high concentrations, SSa first self-aggregates and then dissolves. This is because the solubilization behavior of Ro shifts the precipitation–dissolution equilibrium in the direction of dissolution. These results of the simulations are consistent with those of transmission electron microscopy (TEM) and dynamic light scattering (DLS).

© 2012 Elsevier Inc. All rights reserved.

### 1. Introduction

Biosurfactants are surfactants derived directly from natural sources. They offer advantages over chemical surfactants (also called synthetic surfactants) in that they are derived from renewable sources and are minimally toxic or non-toxic, biodegradable, highly active, often reusable through regeneration, highly specific, and effective under extreme temperature and pH conditions [1–3]. Biosurfactants can self-assemble into rich morphologies, such as micelles, vesicles, and bilayers. They are important in a wide range of technological applications [4–7].

Saponins are plant-derived biosurfactants. They have amphiphilic molecular structures containing a hydrophobic triterpene or steroid aglycone and one or more hydrophilic sugar chains. Increasing consumer demand for natural products coupled with their surfactant properties (such as emulsifying and solubilizing properties) and mounting evidence for their biological activities (including anticancer and anti-cholesterol effects) have led to the successful expansion of commercial applications in the food,

cosmetics, and pharmaceutical sectors [8]. Particularly in the pharmaceutical industry, saponins have been proposed as safe and effective adjuvants to enhance the absorption and dissolution of pharmacologically active substances or drugs through solubilization [9,10]. However, there is no literature on the mechanism underlying the solubilization of saponin despite its importance in the selection and optimization of the formulation of these systems. This limits the applications of saponin.

Many of the herbs used in traditional Chinese medicine (TCM) have been observed to contain saponins, and many saponins have been shown to promote the solubility of insoluble drugs [11–13]. Ginsenoside Ro (Ro), a natural anionic biosurfactant derived from ginseng (roots of *Panax ginseng* C.A. Mey), has been shown to form micelles above the critical micelle concentration (CMC) in aqueous solutions and markedly increase the solubility of saikosaponin a (SSa) which is the active ingredient in *Radix Bupleuri* (roots of *Bupleurum chinense* DC. and *Bupleurum scorzonrifolium* Wild.) but sparingly soluble in water. This is considered one possible mechanism of the synergistic therapeutic effects of ginseng and *Radix Bupleuri*. Ro is a bidesmosidic saponin with two sugar chains linked to a triterpene aglycone: D-glucose and D-glucuronic acid link at C-3. Another D-glucose links at C-28. This special triblock copolymer-like structure causes Ro to self-assemble in aqueous solutions. However, previous studies on Ro have focused only on

\* Corresponding authors. Address: Beijing University of Chinese Medicine, Beijing 100102, China. Fax: +86 10 84738661.

E-mail addresses: shixinyuan01@163.com (X. Shi), yjqiao@263.net (Y. Qiao).

<sup>1</sup> These authors contributed equally to this work.

the influence of medium conditions, such as temperature, pH, and salt concentration on CMC [13]. Colloidal properties such as the morphology and size of the aggregates and the solubilization mechanism are not yet clearly understood.

Mesoscopic simulations were used to promote deeper understanding of the processes by which saponin aggregates and solubilizes. Mesoscopic simulations have been used to study the aggregation behavior of polymeric surfactants before [14–24]. As computing power has increased, mesoscopic simulation has formed a bridge between speedy molecular kinetics and slow thermodynamic relaxation of macroscale properties. It serves as a means of addressing the limitations of existing analytical and experimental approaches [25]. Mesoscopic dynamics (MesoDyn) and dissipative particle dynamics (DPD) are two common methods of mesoscopic simulation. Both methods coarse-grain the familiar atomistic representation of the molecule to gain orders of magnitude in both length and time scale relative to traditional atomistic scale simulation [26]. MesoDyn is based on a dynamic variant of mean-field density functional theory. It has the advantage of allowing the investigation of the microphase separation of block copolymers [27]. DPD is a particle-based method of simulation. It allows soft coarse-grained particles to interact through a simple-wise potential and to thermally equilibrate through hydrodynamics on a mesoscopic scale [28,29]. DPD can accurately capture the hydrodynamic behavior of fluids and the underlying interactions of the species. It can also directly present the movement of meso-molecules, which MesoDyn simulation cannot do.

In this paper, we used both MesoDyn and DPD simulation methods to study the self-aggregation behavior of Ro and the interactions between Ro and Ssa to illustrate the mechanism by which saponin aggregates and solubilizes from different perspectives. The results of our simulation are here compared to experimental results collected using a transmission electron microscope (TEM) and dynamic light scattering (DLS).

## 2. Simulation method

### 2.1. MesoDyn method

MesoDyn is based on a dynamic variant of mean-field density functional theory, which states that there is a one-to-one mapping between the distribution functions of the system, the densities, and an external potential field. The model used in the MesoDyn project consists of a variety of beads whose interactions are described by harmonic oscillator potentials for the intramolecular interactions (Gaussian chain) and a mean-field potential for all other interactions [27]. Each bead represents a certain group of atoms.

The distribution functions of the independent Gaussian chains factorize exactly, and the density function can be simplified to a product of a single-chain density function. In this approximation, the free energy functional can be written as follows:

$$F[\psi] = \frac{1}{Q} \int dR (\psi H^{id} + \beta^{-1} \psi \ln \psi) + F^{nid}[\rho^0] \quad (1)$$

Here, the first term is the average value of the Hamiltonian for internal Gaussian chain interactions; the second term is the free energy functional stems from the Gibbs entropy of the distribution; and the third term is the non-ideal contribution related to the interchain interactions. This last can be written as follows:

$$F^{nid}[\rho] = \frac{1}{2} \sum_{ij} \int_V \int_V \varepsilon_{ij}(|r - r'|) \rho_i(r) \rho_j(r') dr dr' \quad (2)$$

Here,  $\varepsilon_{ij}(|r - r'|)$  is a cohesive interaction defined by the same Gaussian kernel as in the ideal Hamiltonian chain. This parameter is then

directly related to the Flory–Huggins interaction parameter  $\chi$  through the following:

$$\chi_{ij} = \frac{\beta}{2\nu} (\varepsilon_{ij} + \varepsilon_{ij} - \varepsilon_{ii} - \varepsilon_{jj}) \quad (3)$$

In a MesoDyn simulation, the input repulsion parameter is  $\lambda_{ij} = \nu^{-1} \varepsilon_{ij}$ , given in  $\text{kJ mol}^{-1}$ . Rearranging the equation and converting unit gives the following:

$$\lambda_{ij} = \nu^{-1} \varepsilon_{ij} = \chi_{ij} RT \quad (4)$$

Here,  $\chi_{ij}$  is calculated using the Blends module in the commercial software package Materials Studio 4.1 (Accelrys Inc.), and the results are shown in Table 1.

### 2.2. DPD method

(DPD) is a mesoscopic simulation technique suitable to the study of the collective behavior of complex fluids [28,29]. A DPD bead represents a small region of fluid matter and its motion is assumed to be governed by Newton's laws.

$$\frac{d\mathbf{r}_i}{dt} = \mathbf{v}_i \quad m_i \frac{d\mathbf{v}_i}{dt} = \mathbf{f}_i \quad (5)$$

Here,  $\mathbf{r}_i$ ,  $\mathbf{v}_i$ ,  $m_i$ , and  $\mathbf{f}_i$  denote the position vector, velocity, mass, and total force acting on particle  $i$ , respectively.

The force  $\mathbf{f}_i$  between each pair of beads contains three parts: a harmonic conservative interaction force ( $\mathbf{F}_{ij}^C$ ), which is a soft repulsion acting along the line of centers; a dissipative force ( $\mathbf{F}_{ij}^D$ ), which represents the viscous drag between moving beads; and a random force ( $\mathbf{F}_{ij}^R$ ), which maintains energy input into the system in opposition to the dissipation. All forces are short-range with a fixed cut-off radius  $r_c$ , which is usually chosen as the reduced unit of length  $r_c \equiv 1$ . They are given as follows:

$$\mathbf{f}_i = \sum_{j \neq i} (\mathbf{F}_{ij}^C + \mathbf{F}_{ij}^D + \mathbf{F}_{ij}^R) \quad (6)$$

$$\mathbf{F}_{ij}^C = \begin{cases} a_{ij}(1 - r_{ij})\hat{\mathbf{r}}_{ij} & (r_{ij} < 1) \\ 0 & (r_{ij} \geq 1) \end{cases} \quad (7)$$

$$\mathbf{F}_{ij}^D = -\gamma w^D(r_{ij})(\hat{\mathbf{r}}_{ij} \cdot \mathbf{v}_{ij})\hat{\mathbf{r}}_{ij} \quad (8)$$

$$\mathbf{F}_{ij}^R = \sigma w^R(r_{ij}) \xi_{ij} \frac{1}{\sqrt{\Delta t}} \hat{\mathbf{r}}_{ij} \quad (9)$$

Here,  $a_{ij}$  is a maximum repulsion between particle  $i$  and particle  $j$ ;  $\mathbf{r}_{ij} = \mathbf{r}_i - \mathbf{r}_j$ ,  $r_{ij} = |\mathbf{r}_{ij}|$ ,  $\hat{\mathbf{r}}_{ij} = \mathbf{r}_{ij}/|\mathbf{r}_{ij}|$ ;  $\gamma$  is the dissipation strength;  $\sigma$  is the noise strength;  $w^D$  and  $w^R$  are  $r$ -dependent weight functions vanishing for  $r > 1$ ;  $\xi_{ij}$  is a random number with zero mean and unit variance, and  $\Delta t$  is the time step of the simulation.

Combined with the known compressibility of water and binodal data, the following expression can be obtained between  $a_{ij}$  and the Flory–Huggins  $\chi$  parameter:

$$a_{ij} = a_{ii} + 3.27\chi_{ij} \quad (10)$$

**Table 1**  
Interaction parameters used in MesoDyn simulations.

	M	G	GA	N	F	W
M	0					
G	18.63583	0				
GA	21.36526	−0.88555	0			
N	0	18.63583	21.36526	0		
F	10.58693	0.701731	1.639121	10.58693	0	
W	23.61074	3.058319	7.351101	23.61074	12.40741	0

Here,  $a_{ij} = 25k_B T$  at a density  $\rho = N/V = 3$ , and the value of  $k_B T$  is defined as 1. The  $\chi_{ij}$  values can be calculated from the solubility parameters using the following:

$$\chi_{ij} = \frac{(\delta_i - \delta_j)^2 V}{RT} \quad (11)$$

Here,  $V$  is the arithmetic average of molar volumes of beads  $i$  and  $j$ .  $\delta_i$  and  $\delta_j$  are the solubility parameters, which depend on the chemical nature of species and can be obtained through the simulation of molecular dynamics (MD). In this study, solubility parameters are calculated using the Amorphous Cell module in Materials Studio software with the COMPASS force field. The results are shown in Table 2.

### 3. Simulation details

#### 3.1. Models

In both MesoDyn and DPD simulations, the components comprise ginsenoside Ro (Ro), saikosaponin a (SSa), and water. Their chemical structures and corresponding coarse-grained models are shown in Fig. 1. Both Ro and SSa contain a hydrophobic pentacyclic triterpenoid aglycone and several hydrophilic sugars. The aglycone is divided into five identical beads (red M for the aglycone of Ro; purple N for the aglycone of SSa). Each sugar is represented by one bead (green G for glucose; blue GA for glucuronic acid; cyan F for fucose). One water molecule is represented by one bead (pink W for water). All these beads have the same volume. To show aggregate morphologies clearly, the display styles were chosen so that all water beads were hidden in both MesoDyn and DPD simulations.

#### 3.2. Input parameters

In our study, the input parameters for the MesoDyn simulation were chosen as follows: The dimensions of the simulation lattice were  $32 \times 32 \times 32 \text{ nm}^3$ ; the bond length was 1.1543 nm to ensure isotropy of all grid-restricted operators; all bead diffusion coefficients were  $1.0 \times 10^{-7} \text{ cm}^2/\text{s}$  to ensure a stable numerical algorithm, as an approximation; the length of each time step was 50 ns; the total simulation time was 30,000 steps (i.e., 1.5 ms); the simulation temperature was 298 K; the noise-scaling parameter was 100, and the compressibility parameter was fixed at 10.0. Because Ro exists in plants as a salt and can be considered a natural anionic surfactant, the Donnan electrostatic method was applied in the simulation and the salt strength was fixed at  $0.01 \text{ mol l}^{-1}$  [14,30,31].

In the DPD simulation, a  $20 \times 20 \times 20 r_0^3$  cubic box was chosen, which was proved enough to avoid the finite size in our pre-test (Fig. S1). The time step was  $0.05 t_0$  and the total simulation involved 30,000 steps. This was long enough for the simulation system to reach equilibrium (Fig. S2).  $r_0$  and  $t_0$  are DPD length and time unit, respectively. In this work, the average volume of beads was  $210 \text{ \AA}^3$ . Because a cube of  $r_0^3$  contained three beads ( $\rho r_0^3 = 3$ ),  $r_0$  was calculated to be  $r_0 = \sqrt[3]{3 \times 210 \text{ \AA}^3} = 8.57 \text{ \AA}$ . The time unit

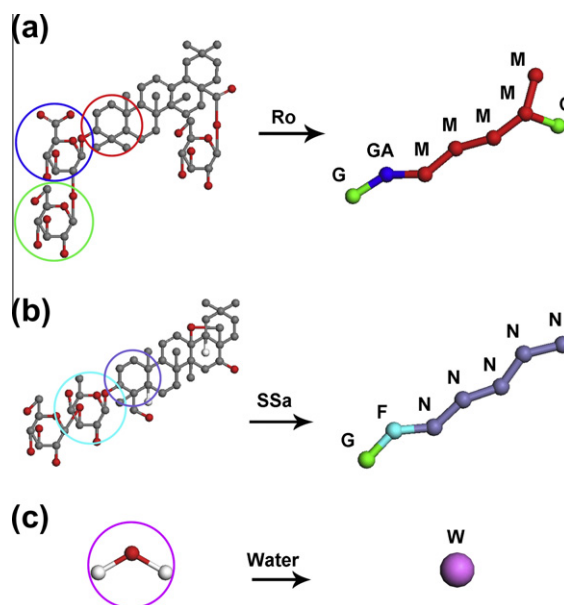


Fig. 1. Chemical structures and coarse-grained models: (a) ginsenoside Ro (Ro), (b) saikosaponin a (SSa), (c) water.

$t_0 = r_0 \sqrt{m_0/k_B T} = 0.006 \text{ ns}$  where  $m_0 = 126 \text{ amu}$  was the average mass of beads. Although the time and length of our simulations could not quantitatively relate to the physical systems, the structural transformation still provided a great deal of useful qualitative information, which may improve our understanding of the solubilization mechanism of saponin. The spring constant was fixed at 4.0, which has been found to give reasonable results in our study system [27]. The electrostatic interactions of the beads were contained in the repulsion parameters calculated by using MD simulation.

Both MesoDyn and DPD simulations started from a randomly dispersed condition.

### 4. Experiment

#### 4.1. Materials

SSa and Ro were purchased from Vicks biotechnology Co., LTD (98% purity). The saturated solutions of SSa and SSa in 0.1% Ro were prepared by dissolving excess SSa in water and 0.1% Ro solution, respectively, at  $25^\circ \text{C}$  for 24 h, and then, the solutions were filtered through a  $0.45 \text{ \mu m}$  Millipore filter.

#### 4.2. Transmission electron microscopy (TEM)

The aggregate morphologies of 0.1% Ro solution, saturated SSa solution, and saturated SSa solution in 0.1% Ro were observed on a transmission electron microscope (TEM, JEOL JEM-1230 microscope) operated at an acceleration voltage of 80 kV. The solution samples were deposited onto copper grids that had been precoated with a thin film of formvar and then coated with a thin carbon film. The liquid was blotted off with filter paper after a few minutes, and the grids were air-dried.

#### 4.3. Dynamic light scattering (DLS) measurement

The sizes of the aggregates were measured with a Zetasizer Nano ZS dynamic light scattering (DLS) instrument (Malvern, UK) at an angle of  $173^\circ$  at  $25^\circ \text{C}$ .

Table 2  
Repulsion parameters used in DPD simulations.

	M	G	GA	N	F	W
M	25					
G	83.37862	25				
GA	433.4031	175.7504	25			
N	25	83.37862	433.4031	25		
F	57.26385	28.79447	228.968	57.26385	25	
W	123.7055	39.70408	55.32322	123.7055	53.71722	25

## 5. Results and discussion

### 5.1. Self-aggregation behavior of Ro in aqueous solution

#### 5.1.1. MesoDyn simulation results

In the MesoDyn simulation, Ro started to aggregate at 1.3 vol%. The time evolutions of order parameters for 1.3 vol% Ro, the corresponding mesostructures, and their section views are shown in Fig. 2. The order parameter  $P_I$  is defined as the volume average of the difference between the local density squared and the overall density squared [27]:

$$P_I = \frac{1}{V} \int_V [\eta_i^2(r) - \eta_i^2] dr \quad (12)$$

Here,  $\eta_i$  is a dimensionless density (volume fraction) for species  $i$ . Order parameters with large values indicate strong phase segregation.

As shown in Fig. 2a, the process of aggregation could be divided into three stages. The first stage was the pre-formation stage, during which the order parameter  $P_I$  changed little and the system was in the homogeneous state (0–13,600 steps). At 13,600 steps,  $P_I$  values started to increase rapidly, reaching a maximum at 13,670 steps. Then,  $P_I$  values decreased until the system reached 13,800 steps. This was the formation stage (13,600–13,800 steps). During this stage, spherical aggregates were formed and they increased in size over time, as shown in Fig. 2b–e. The aggregate core changed from a completely hydrophobic structure to a structure including hydrophilic beads. This is a typical vesicle structure. The density distribution curves of different beads in the vesicles are presented in Fig. S3. Changes in core structure occurred at exactly 13,670 steps, which may be why the maximum  $P_I$  value appeared at this time. However, the mechanism underlying these changes could not be seen directly from the MesoDyn simulation. The third stage was the equilibrium stage, during which both the order parameter

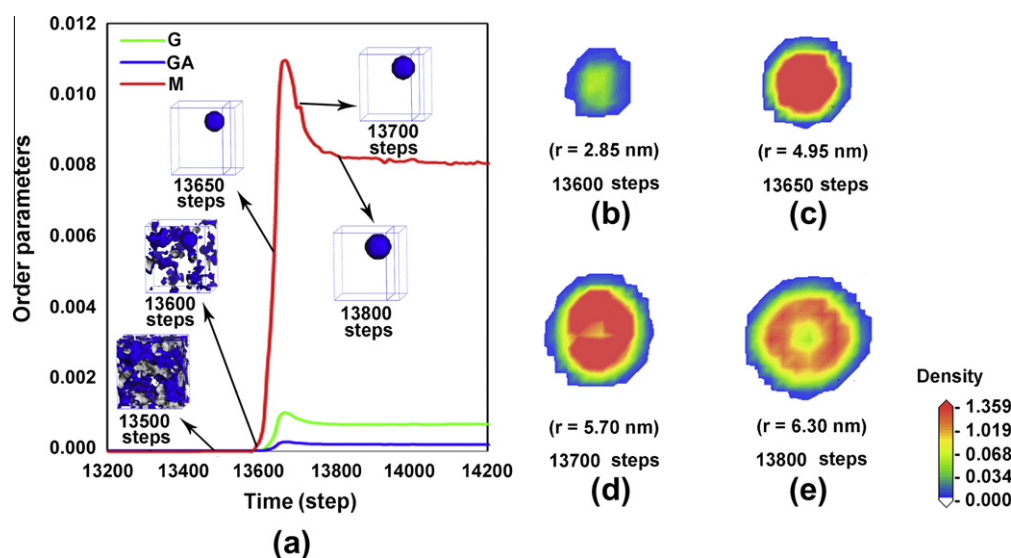


**Fig. 2.** Variation of order parameters over time for 1.3 vol% Ro and corresponding mesostructures and section views. (a) order parameters and mesostructures at different times, (b–e) section views of the density distribution of hydrophobic bead M at corresponding times.

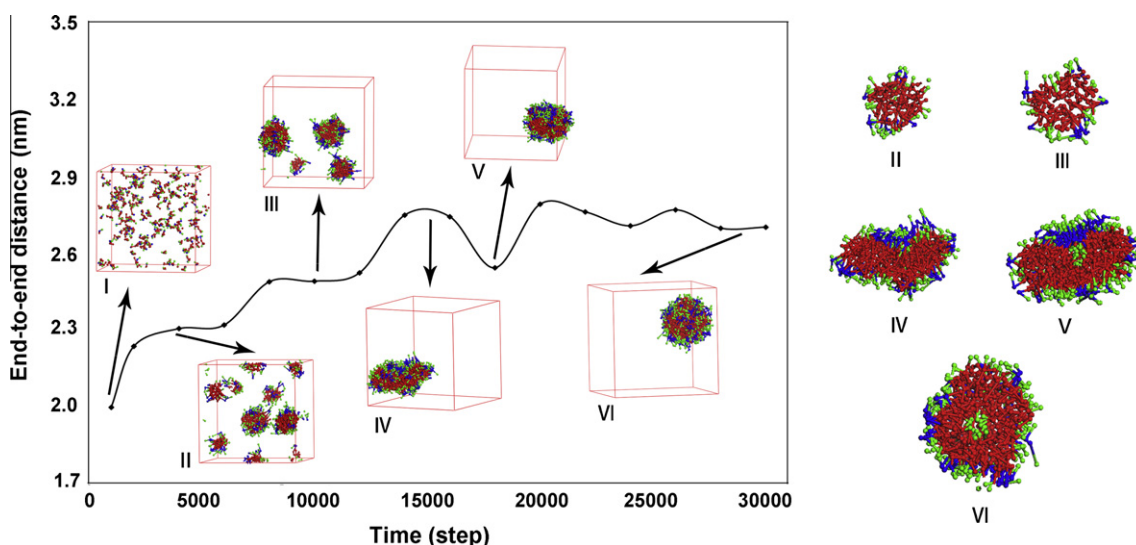


**Fig. 3.** Variations in end-to-end distance over time and corresponding mesostructures and section views. (a) end-to-end distance and mesostructures during different stages, (b–e) section views of typical aggregations in corresponding stages.



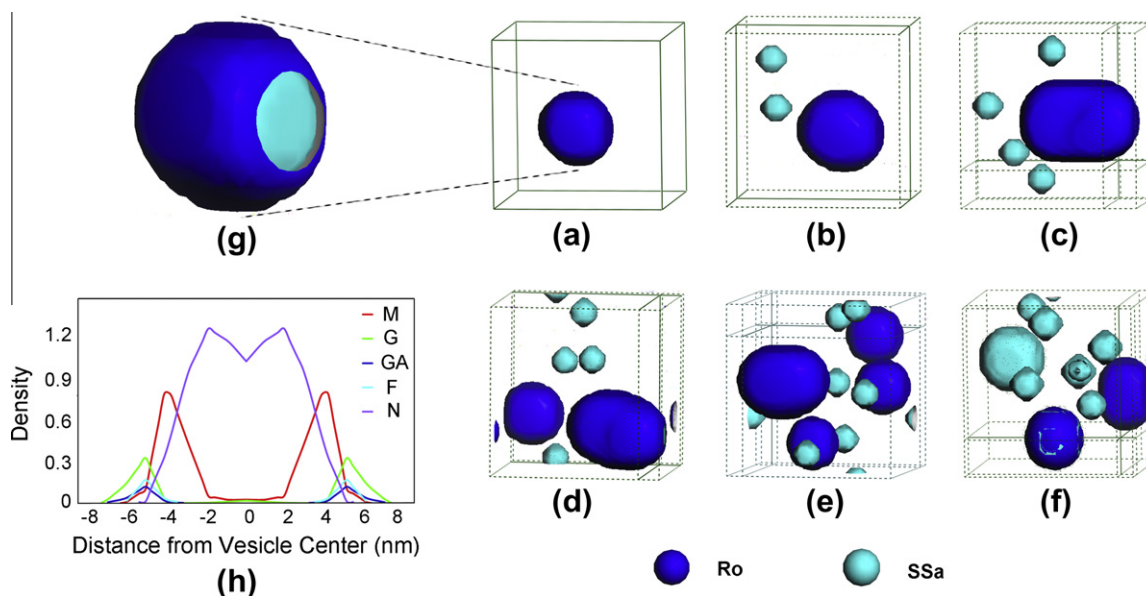


**Fig. 4.** Mesostructure evolution of 1.3 vol% Ro and different concentrations of SSa blend system. (a) 1.0 vol% SSa, (b) 3.0 vol% SSa, (c) 4.0 vol% SSa, (d) 4.1 vol% SSa, (e) 4.4 vol% SSa, (f) 4.5 vol% SSa, (g) section view of the mesostructure in (a), (h) density distribution curves of different beads of the mesostructure in (a).

and the vesicle morphology were largely maintained (>13,800 steps).

#### 5.1.2. DPD simulation results

The MesoDyn simulation results show the phase separation process of Ro directly. They indicate that Ro can form vesicles in aqueous solutions. To give a more visualized understanding of the vesicle formation process, the DPD method was used to simulate the self-aggregation behavior of Ro. End-to-end distance is a concept derived from polymers. It is defined as the distance between one end of the polymer chain and the other, and it is used to describe the degree of curliness of the polymer chain. To show the changes in the mesoscopic morphologies that occur during vesicle formation, the variations in end-to-end distance over time and the corresponding mesostructures and section views are given in Fig. 3.

The process of vesicle formation could be subdivided into six stages. Stage I was the pre-formation stage, during which Ro molecules dispersed randomly in water. The end-to-end distance of the molecules remained small during this stage because of the strong repulsive forces between hydrophobic beads M and W, which forced the hydrophobic aglycone to contract. Stages II–V were the formation stages, in which the end-to-end distance increased periodically. Ro molecules were found to aggregate into many small spheres (stage II) and then merge into large ones (stage III). The end-to-end distance increased because of the increasing size of the aggregates and the fact that the expanded Ro molecules occupied more space. Then, during stage IV, the large spheres merged to form an oblate membrane, which closed up to form a spherical vesicle at stage V. The end-to-end distance decreased because, during the closing process, the surface molecules were compressed in the closing direction. After that, the compressed molecules diffused and stretched within the vesicle to reach an equilibrium state. This caused the end-to-end distance to increase again. This formation process is similar to that of amphiphilic triblock copolymers, as has been verified in previous studies [32–34]. It also explains the changes in core structure indicated in the MesoDyn simulation. Stage VI was found to be the equilibrium stage. The section view of this stage clearly shows the structure of the vesicles, showing two hydrophilic regions, one in the core

and another on the surface. Glucuronic acid (GA) beads were located very close to the surface because of their strong hydrophilicity. The electrostatic repulsion caused by dissociated carboxyls from GA may have contributed to vesicle stability.

#### 5.2. Solubilization mechanism of SSa by Ro

Vesicles have been widely studied as drug carriers. They can increase the solubility of otherwise insoluble drugs [35–40]. Because Ro can form vesicles, it is rational to assume that SSa molecules are solubilized into Ro vesicles, causing marked increases in the solubility of SSa. However, the results of the present simulations indicate that the solubilization mechanism of SSa by Ro is more complex, considering that SSa is also a type of saponin and that it contains a hydrophobic aglycone and a hydrophilic sugar chain and has surface activity.

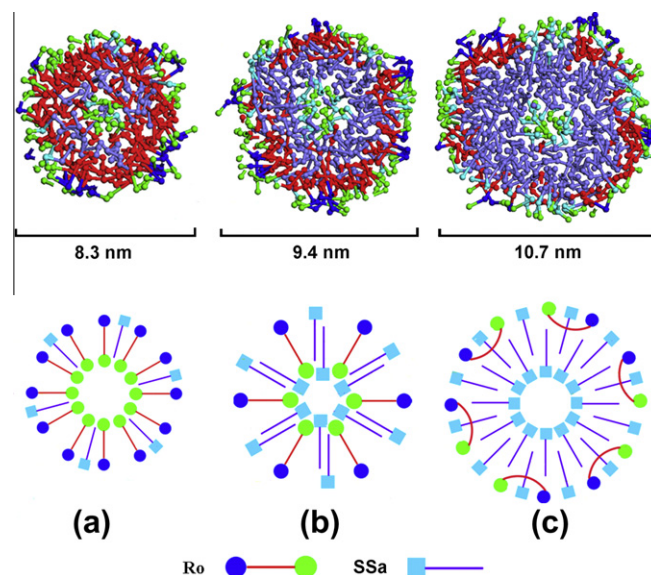


**Fig. 5.** Section views of 5.0 vol% Ro vesicles with different concentrations of SSa in DPD simulation and their schematic drawings. (a) 1.0 vol% SSa, (b) 2.0 vol% SSa, (c) 5.0 vol% SSa.

### 5.2.1. Effect of concentration of SSa on aggregation behavior of blended Ro and SSa systems

To determine the effects of SSa concentration, Ro was fixed at 1.3 vol%, the concentration at which Ro could form vesicles. The results shown in Fig. 4 indicate that SSa molecules could be solubilized into Ro vesicles. The solubilization site within the vesicles

was found to be close to the palisade layer and core (Fig. 4g and h). As the concentration of SSa increased, the Ro vesicles grew from spherical vesicles into short rod-like vesicles (Fig. 4a–c). However, SSa, which is strongly hydrophobic, tended to inhibit the growth of the Ro vesicles [41]. As a result, as SSa concentration increased further, the number rather than the size of Ro vesicles increased (Fig. 4d and e). The simulation results also indicate that, at low concentrations, SSa molecules were completely solubilized into the Ro vesicles (Fig. 4a). However, as the concentration increased, SSa self-aggregated outside the Ro vesicles (Fig. 4b–f). When the concentration reached 4.5 vol%, the solubilization capacity of Ro on SSa no longer increased. SSa started to form large aggregates in the aqueous solution (Fig. 4f).

The DPD simulation results shown in Fig. 5 and Fig. S4 provide visualized and quantified insights into the variations in solubilization site of SSa in the Ro vesicles as SSa concentration increased. At low concentrations, SSa molecules were found to be solubilized in the palisade layer of the Ro vesicles. The hydrophobic aglycones of SSa molecules were inserted into the palisade layer formed by the aglycones of Ro molecules, and the sugars of SSa were located on the surface to interact with the sugars of Ro through hydrogen bonding or dipolar interaction (Fig. 5a). As the concentration of SSa increased, Ro and SSa interacted with each other to form mixed vesicles. SSa molecules were preferentially absorbed into the vesicles and located closer to the core due to their stronger hydrophobicity [37]. The density of the beads N in this area increased with SSa concentration. The sugars of SSa were encapsulated into the vesicles at the same time (Fig. 5b). Within a certain SSa concentration range, vesicle volume increased as concentration increased, as found in the MesoDyn simulation (Fig. 4a and b). However, at high concentrations, SSa occupied the vesicle core to form the main part

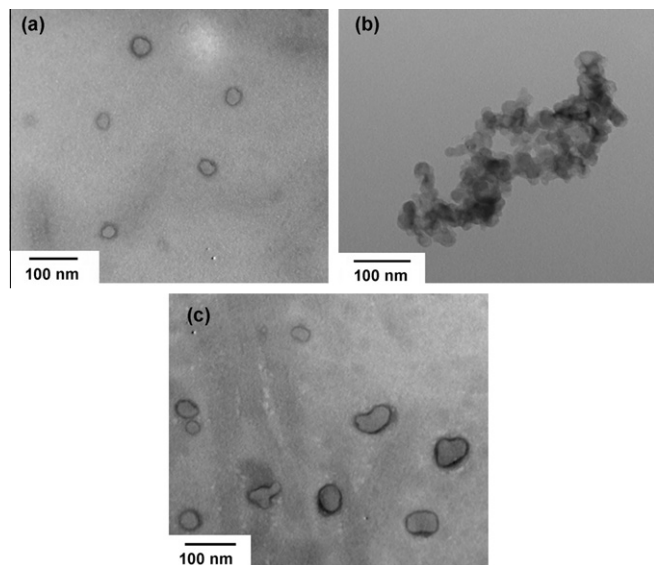


**Fig. 6.** TEM images of Ro vesicles, SSa aggregates, and Ro-SSa mixed vesicles. (a) Ro vesicles, (b) SSa aggregates, (c) Ro-SSa mixed vesicles.

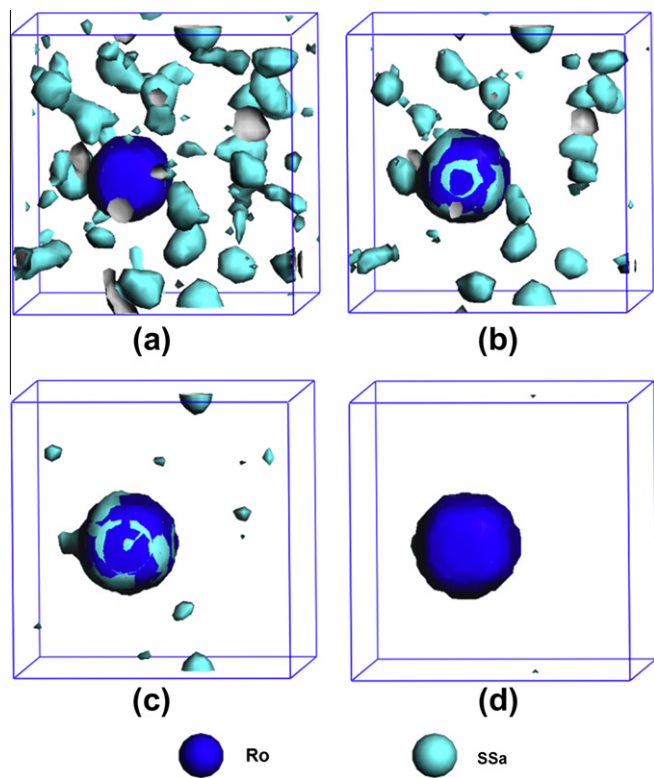


**Fig. 7.** Snapshots of solubilization process of 1.0 vol% SSa by 1.3 vol% Ro. (a) 2,540 steps, Ro molecules aggregated preferentially to form spherical vesicles while SSa molecules dispersed in a disordered manner. (b) 2,550 steps, SSa molecules were gradually absorbed into Ro vesicles. (c) 2,580 steps, SSa were almost completely absorbed into Ro vesicles. (d) 2,610 steps, SSa were totally absorbed into Ro vesicles.

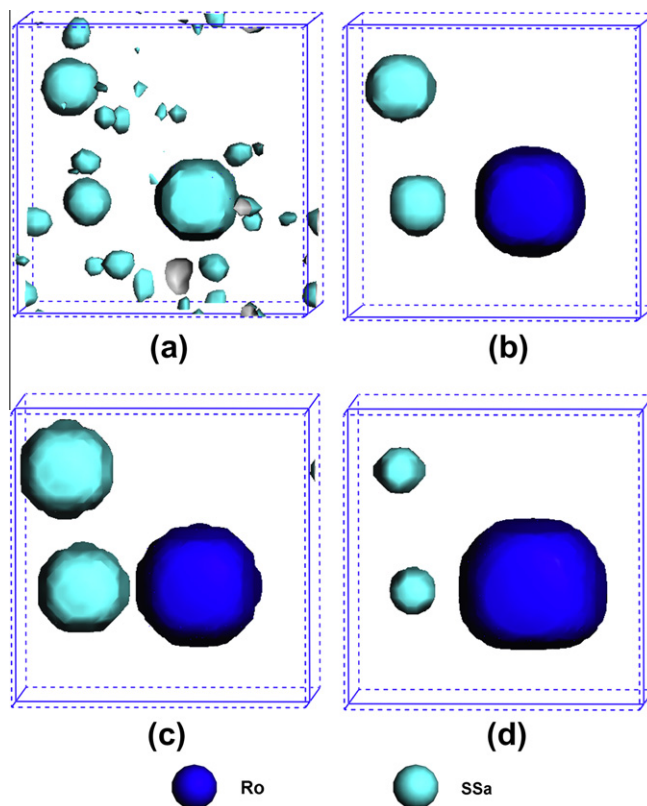


**Fig. 8.** Snapshots of solubilization process of 3.0 vol% SSa by 1.3 vol% Ro. (a) 380 steps, SSa molecules self-aggregated to form small aggregates. (b) 400 steps, Ro packed SSa cores to form mixed vesicles. (c) 600 steps, both the Ro vesicles and unpacked SSa aggregates grew in size. (d) 2,600 steps, mixed vesicles continued to grow but the sizes of SSa aggregates was reduced.

of the mixed vesicle, with Ro molecules adsorbed on the surface because the hydrophilic sugars at either ends of Ro could not pass through the hydrophobic layer formed by the aglycone of SSa to reach the vesicle core (Fig. 5c). As discussed in Section 5.1.2, glucuronic acid (GA) beads of Ro were found on vesicle surfaces. They stabilized the vesicles through their strong hydrophilicity and electrostatic repulsion properties.

The aggregate morphologies of 0.1% Ro solution, SSa saturated solution, and a saturated solution of SSa in 0.1% Ro were observed using TEM (Fig. 6). Ro self-aggregated into spherical vesicles with diameters ranging from 30 nm to 50 nm (Fig. 6a). However, SSa self-aggregated into spherical micelles. This is consistent with the results of our simulation (Fig. S5). The small SSa micelles collided with each other to form large fractal aggregates because of their strong hydrophobicity. Their diameters were above 300 nm (Fig. 6b). As a result, SSa tended to precipitate in aqueous solutions. When SSa was added to the Ro solution, larger vesicles with diameters of 50–100 nm appeared (Fig. 6c). This may be because

SSa was solubilized into Ro vesicles to form mixed vesicles, as described in our simulation.

### 5.2.2. Process of solubilization of SSa by Ro

The phase behavior variation for 1.3 vol% Ro and different concentrations of SSa in blended systems is shown in Figs. 7 and 8. The solubilization process varied with SSa concentration.

At low concentrations (1.0 vol% SSa), Ro molecules aggregated preferentially to pack a few SSa molecules to form spherical vesicles, but most of the SSa molecules dispersed in a disordered manner because the concentration was too low for SSa to self-aggregate in aqueous solutions (Fig. 7a). Under these conditions, SSa molecules were gradually absorbed into Ro vesicles (Fig. 7b and c) until all the SSa molecules were solubilized (Fig. 7d). This can explain the palisade layer solubilization of SSa at low concentrations.

However, at high concentrations (3.0 vol% SSa), the solubilization process is different. It can be divided into four stages. During the first stage, SSa, not Ro, preferentially self-aggregated to form small aggregates. This was because of its strong hydrophobicity (Fig. 8a). Then, Ro packed SSa aggregates into mixed vesicles (Fig. 8b). It is worth noting that the time required for Ro to aggregate (400 steps) was much shorter than that at low SSa concentrations (2,540 steps). The variation of time required for Ro to aggregate is plotted versus the SSa concentration in Fig. 9. In this way, insoluble substances that can aggregate in aqueous solutions to form hydrophobic cores were found to induce the aggregation of surfactants and accelerate the phase separation process of blend system.

During the third stage, as time passed, both the mixed vesicles and unpacked SSa aggregates increased in size. This was because the concentration of both was dense enough for both of them to aggregate (Fig. 8c). However, during the fourth stage, only the mixed vesicles continued to grow in size; the SSa aggregates shrank (Fig. 8d). This might be because the solubilization of SSa

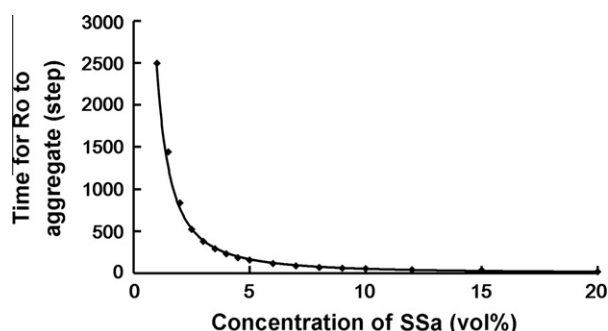


Fig. 9. Time required for Ro to aggregate versus concentration of SSa.

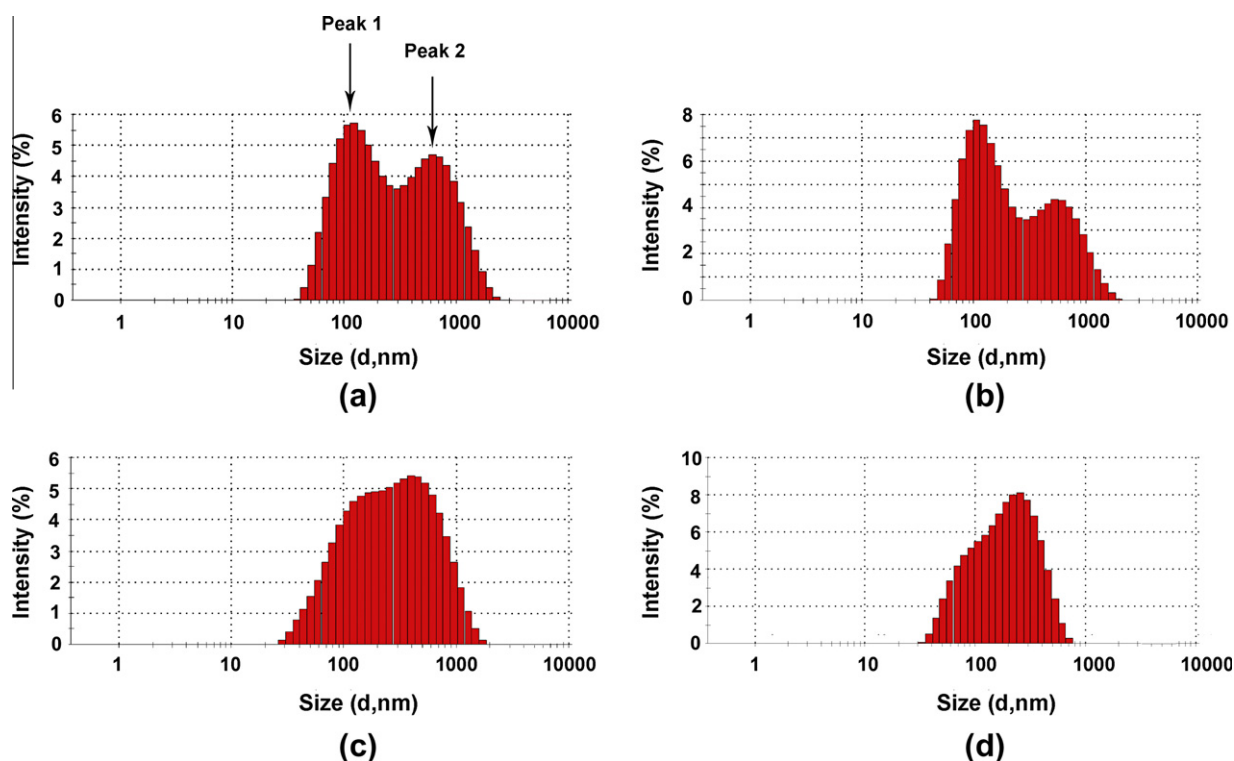


Fig. 10. Dynamic light scattering (DLS) of 1 ml 0.1% Ro solution with 0.1 ml SSa saturated solution added at different times. (a) 0 min, (b) 10 min, (c) 20 min, (d) 60 min.



by Ro causes the precipitation–dissolution equilibrium of SSa shift toward dissolution.

To corroborate the results of these simulations, 0.1 ml SSa saturated solution was added to 1 ml 0.1% Ro solution, and the variations in the sizes of the aggregates in this blended system over time were measured using DLS. The results are shown in Fig. 10. As controls, 0.1 ml SSa saturated solution was added to 1 ml water (group 1) and 0.1 ml water was added to 1 ml 0.1% Ro solution (group 2). The results are shown in Fig. S6. Peak 1 occurred at 175.2 nm. It was mainly attributable to the Ro vesicles, and peak 2, which occurred at 719.7 nm, was mainly attributable to the SSa aggregates. Over time evolution, peak 1 moved to the right and peak 2 moved to the left, indicating that the size of the Ro aggregates increased and the size of the SSa aggregates decreased. The two peaks finally merged into one peak and the final diameter value was 213.6 nm. This was larger than the value of the Ro solution without SSa (202.9 nm) but smaller than the size of SSa aggregates at this moment (407.9 nm). All these results indicate that SSa could be solubilized into Ro vesicles and increase the sizes of those vesicles. The results are consistent with our simulation. However, the diameter values obtained from the TEM measurements are slightly smaller than those from DLS. This may have been because the TEM samples had been air-dried. The solvent evaporation led to the shrinkage, collapse, and even destruction of large aggregates, which resulted in the size reduction [42].

## 6. Conclusion

In this paper, ginsenoside Ro was used as a model object, and saponin was proven to form vesicles for the first time. The formation pathway may occur via the closure of oblate membranes. To our knowledge, there has been little research into the morphologies of saponin aggregates, and only spherical and wormlike micelles have been observed previously [43,44]. This discovery not only broadens our knowledge of the self-assembly behavior of saponin but it may also expand the potential applications of saponin in drug delivery systems.

Here, Ro vesicles were proven to solubilize SSa by both simulation and experimental methods. The effect of the concentration of SSa on the aggregation behavior of blended Ro and SSa systems indicated that, as concentration increased, the solubilization site of SSa varied from the palisade layer to the vesicle core. Glucuronic acid (GA) beads of Ro were always located on vesicle surface, where they stabilized the vesicles through their strong hydrophilicity and electrostatic repulsion. That may be why glucuronide moiety is so important to the solubilization effect that Ro has on SSa [45]. By studying the solubilization process of Ro at different SSa concentrations, it was shown that insoluble substances could form hydrophobic cores in aqueous solution, causing aggregation of the surfactant. This accelerated the phase separation process of blended systems. Considering that SSa is also a kind of biosurfactant which can form mixed vesicles with Ro, the conclusion can also be extended to explain the dominant role of the more hydrophobic surfactants in the mixed surfactant systems to accelerate phase separation and reduce the critical micelle concentration (CMC) [41].

By employing mesoscopic simulations and experimental methods, we are able to understand the solubilization behavior of saponin at the mesoscale. The results not only broaden our knowledge of saponin biosurfactant, but also act as guidance for the applications of saponin in the pharmaceutical industry.

## Acknowledgments

This work was financially supported by the National Natural Science Foundation of China (81073058) and Innovation Team Foundation of Beijing University of Chinese Medicine, Beijing (2011-CXTD-11, Research Center of TCM-information Engineering).

## Appendix A. Supplementary material

Supplementary data associated with this article can be found, in the online version, at <http://dx.doi.org/10.1016/j.jcis.2012.06.018>.

## References

- [1] Q.Y. Xu, M. Nakajima, Z.S. Liu, T. Shiina, *Int. J. Mol. Sci.* 12 (2011) 462.
- [2] L. Rodrigues, I.M. Banat, J. Teixeira, R. Oliveira, *J. Antimicrob. Chemoth.* 57 (2006) 609.
- [3] K. Urum, T. Pekdemir, *Chemosphere* 57 (2004) 1139.
- [4] J. Penfold, R.K. Thomas, H.-H. Shen, *Soft. Matter* 8 (2012) 578.
- [5] H. Jian, X. Liao, L. Zhu, W. Zhang, J. Jiang, *J. Colloid Interface Sci.* (2011).
- [6] J.S. Clifford, M.A. Ioannidis, R.L. Legge, *J. Colloid Interface Sci.* 305 (2007) 361.
- [7] M. Sanchez, F.J. Aranda, M.J. Espuny, A. Marques, J.A. Teruel, A. Manresa, A. Ortiz, *J. Colloid Interface Sci.* 307 (2007) 246.
- [8] O. Guclu-Ustundag, G. Mazza, *Crit. Rev. Food Sci.* 47 (2007) 231.
- [9] O. Tanaka, N. Yata, Google Patents, United States, 1985.
- [10] S. Tsuzaki, S. Wanezaki, H. Araki, Google Patents, United State, 2008.
- [11] U. Walthelm, K. Dittrich, G. Gelbrich, T. Schoepke, *Planta Med.* 67 (2001) 49.
- [12] Y. Sasaki, K. Mizutani, R. Kasai, O. Tanaka, *Chem. Pharm. Bull.* 36 (1988) 3491.
- [13] H. Kimata, N. Sumida, N. Matsufuji, T. Morita, K. Ito, N. Yata, O. Tanaka, *Chem. Pharm. Bull.* 33 (1985) 2849.
- [14] L.S. Zheng, Y.Q. Yang, X.D. Guo, Y. Sun, Y. Qian, L.J. Zhang, *J. Colloid Interface Sci.* 363 (2011) 114.
- [15] J.-Y. Pang, X. Lue, J. Zhang, S.-L. Yuan, G.-Y. Xu, *Acta Phys. Chim. Sin.* 27 (2011) 520.
- [16] X.R. Cao, G.Y. Xu, S.L. Yuan, B.Y. Gao, *Soft. Matter* 7 (2011) 9035.
- [17] Y.M. Li, Y.Y. Guo, M.T. Bao, X.L. Gao, *J. Colloid Interface Sci.* 361 (2011) 573.
- [18] P. Posocco, M. Fermeglia, S. Pricl, *J. Mater. Chem.* 20 (2010) 7742.
- [19] Y. Li, G. Xu, Y. Zhu, Y. Wang, H. Gong, *Colloid Surf. A-Physicochem. Eng. Asp.* 334 (2009) 124.
- [20] Z.X.Q.Y. Shi-Ling, X.U.G.Y.L.I.U. Cheng-Bu, *Acta Physico-Chim. Sin.* (2007) 02.
- [21] M.R. Wang, N. Pan, J.K. Wang, S.Y. Chen, *J. Colloid Interface Sci.* 311 (2007) 562.
- [22] A. Maiti, J. Wescott, G. Goldbeck-Wood, *Int. J. Nanotechnol.* 2 (2005) 198.
- [23] Y.M. Lam, G. Goldbeck-Wood, C. Boothroyd, *Mol. Simul.* 30 (2004) 239.
- [24] M. Whittle, E. Dickinson, *J. Colloid Interface Sci.* 242 (2001) 106.
- [25] J. Koelman, P.J. Hoogerbrugge, *Europhys. Lett.* 21 (1993) 363.
- [26] F. Case, P. Alexandridis, A.C.S.D.O.P. Chemistry, A.C.S.D.O. Colloid, S. Chemistry, A.C.S. Meeting, Mesoscale Phenomena in Fluid systems, ACS Publications, 2003.
- [27] J. Fraaije, B.A.C. vanVlimmeren, N.M. Maurits, M. Postma, O.A. Evers, C. Hoffmann, P. Altevogt, G. GoldbeckWood, *J. Chem. Phys.* 106 (1997) 4260.
- [28] P.J. Hoogerbrugge, J. Koelman, *Europhys. Lett.* 19 (1992) 155.
- [29] R.D. Groot, P.B. Warren, *J. Chem. Phys.* 107 (1997) 4423.
- [30] S. Yang, S. Yuan, X. Zhang, Y. Yan, *Colloids Surf. A* 322 (2008) 87.
- [31] A. Kyrilyuk, J. Fraaije, *J. Chem. Phys.* 121 (2004) 2806.
- [32] S. Yamamoto, Y. Maruyama, S. Hyodo, *J. Chem. Phys.* 116 (2002) 5842.
- [33] Y.Y. Han, H.Z. Yu, H.B. Du, W. Jiang, *J. Am. Chem. Soc.* 132 (2010) 1144.
- [34] J.C. Shillcock, *Langmuir* 28 (2012) 541.
- [35] H.J. Lim, E.C. Cho, J. Shim, D.H. Kim, E.J. An, J. Kim, *J. Colloid Interface Sci.* 320 (2008) 460.
- [36] G. Liu, Q. Jin, X. Liu, L. Lv, C. Chen, J. Ji, *Soft. Matter* 7 (2010) 662.
- [37] M.M.A. Elsayed, O.Y. Abdallah, V.F. Naggar, N.M. Khalafallah, *Int. J. Pharm.* 332 (2007) 1.
- [38] L.F. Pacheco, A.M. Carmona-Ribeiro, *J. Colloid Interface Sci.* 258 (2003) 146.
- [39] G. Cevc, *Adv. Drug Deliv. Rev.* 56 (2004) 675.
- [40] I.F. Uchegbu, S.P. Vyas, *Int. J. Pharm.* 172 (1998) 33.
- [41] K. Holmberg, B. Jo nsson, B. Kronberg, B.E. Lindman, *Surfactants and Polymers in Aqueous Solution*, second ed., John Wiley and Sons, 2002.
- [42] Y. Mai, Y. Zhou, D. Yan, *Macromolecules* 38 (2005) 8679.
- [43] M.P.G. Peixoto, J. Treter, P.E. de Resende, N.P. da Silveira, G.G. Ortega, M.J. Lawrence, C.A. Dreiss, *J. Pharm. Sci.* 100 (2011) 536.
- [44] S. Mitra, S.R. Dungan, *J. Agric. Food Chem.* 45 (1997) 1587.
- [45] K. Watanabe, H. Fujino, T. Morita, R. Kasai, O. Tanaka, *Planta Med.* 54 (1988) 405.